

A Novel Deep Learning-based Modelling Strategy from Image of Particles to Mechanical Properties for Granular Materials with CNN and BiLSTM

Pin ZHANG¹ and Zhen-Yu YIN^{1,*}

¹ Department of Civil and Environmental Engineering, Hong Kong Polytechnic University, Hung Hom, Kowloon, Hong Kong, China

* Corresponding author, E-mail: zhenyu.yin@polyu.edu.hk; Tel: +852 3400 8470; Fax: +852 2334 6389

Abstract: It will be practically useful to know the mechanical properties of granular materials by only taking a photo of particles. This study attempts to deal with this challenge by developing a novel deep learning-based modelling strategy. In this strategy, the convolutional neural network (CNN) as image identification algorithm is first used to extract the particle information (particle size distribution PSD and morphology) based on the image of a granular sample, and the bidirectional long short-term memory (BiLSTM) neural network is employed to train the model of reproducing mechanical behaviours and induced fabric evolutions of the sample with corresponding particle information. The datasets of images of samples are generated using discrete element method, and the datasets of mechanical properties together with fabric evolutions are obtained through numerical tests on corresponding samples. As a preliminary attempt, two-dimensional biaxial samples and tests with initially isotropic fabric are considered for the sake of simplicity. The feasibility and reliability of the proposed modelling strategy are evaluated through training and testing. All results indicate that the first part of the model based on CNN is capable of accurately identifying PSD of a granular sample, as well as circularity and roundness of particles, using which as connecting parameters the mechanical behaviours together with induced fabric evolutions of granular materials are subsequently well captured by the second part of the model based on BiLSTM. This study provides a basis and a possible way to obtain immediately particle and packing information, mechanical properties and fabric evolutions by leveraging images of granular materials.

Keywords: Granular material; deep learning; discrete element method; particle morphology; particle size distribution; fabric anisotropy

1. Introduction

The physical and mechanical behaviours of granular materials are complex, because such materials are composed of distinct solid particles interacting with one another [1], which means that the behaviours of granular materials are primarily affected by their particle interactions particularly relating to the particle size distribution (PSD) [2-6] and the particle morphology [7-12]. Experimental tests tend to explain the behaviours of granular materials and investigate the effects of various factors from the macroscopic viewpoint [13-16], but the measurements are expensive using various advanced experimental techniques [17]. Analytical methods derived from continuum mechanics are generally based on strong assumptions with complicated mathematical formulations and myriad parameters which poses great difficulty for engineers in practice. If there is a way through recognizing individual particles and packing assembles to know the mechanical behaviour of the granular material, it will be genius and practically useful. The rapid development and application of deep learning (DL) nowadays bring a dawn for this.

Recently, the application of DL, e.g. convolutional neural network (CNN) and long short-term memory (LSTM), to simulate various properties of materials has gained great attention owing to its strong non-linear mapping capacity [18, 19]. CNN and its variants can directly extract microscopic information from images. Thereby, they have been applied to acquire properties from images of the studied material, such as the evaluation of permeability of porous media [20] and the prediction of fracture evolution of brittle material [21]. LSTM and its variants are characterized by sequence prediction, in which the historical information can be stored and learned. They have thus been successfully employed to simulate path-dependent behaviours of granular materials [22, 23] and demonstrated superior performance than other machine learning algorithms [24]. However, the current application of DL to identify the particle information of material such as the study of PSD and particle morphology is limited, and DL to model macroscopic

1 behaviours is typically only based on results of stress-strain without relating to particle and inter-particle
2
3 information. Therefore, the feasibility of DL-based mechanical modelling with detecting particle
4
5 information only upon images of granular materials deserves to be investigated. If do so, both experimental
6
7 and computational costs can be significantly reduced for engineering practice.
8
9

10
11
12 For such purpose the datasets creation with both micro and macro information is necessary. The
13
14 idealist method is to use Micro-Computed Tomography with performing mechanical tests on real granular
15
16 materials [25-27]. Indeed as a preliminary attempt of the DL-based modelling strategy from image of
17
18 particles of a sample to mechanical properties, two-dimensional (2D) discrete element method (DEM) well
19
20 capturing granular mechanics in an analogous but simplified manner may also be a good choice. Note that
21
22 DEM is a widely applied method to simulate behaviours of granular materials with providing physics
23
24 insight for granular mechanics [1, 28-32]. Besides, the numerical tests eliminate experimental errors due to
25
26 artificial operation or machine problems. DEM itself is computationally expensive on mechanical
27
28 modelling [33], but this disadvantage can be eliminated by DL-based modelling if the datasets of DEM
29
30 simulations are prepared in advance.
31
32
33
34
35
36
37
38
39
40

41
42 Therefore, in this study a novel DL-based strategy for recognising the particle information and
43
44 behaviours of granular materials from image of particles is proposed. The results of DEM-based numerical
45
46 biaxial tests with various particle size distributions and particle morphologies are converted into the
47
48 auxiliary training and testing data. The proposed strategy includes two parts: CNN is first employed to
49
50 identify the particle information including PSD and morphology, followed by BiLSTM to describe the
51
52 mechanical behaviours and induced fabric evolutions of granular materials.
53
54
55
56
57
58
59
60
61
62
63
64
65

2. Generalization of applied methods

2.1 Indicators of particle and packing assembly

Myriad factors control the mechanical behaviour of granular materials, in which only the PSD and particle morphology, as two key fundamental factors, are selected for the sake of simplicity. PSD is computed based on the sizes of all individual particles, and the particle morphology is represented by its circularity and roundness in this study (Fig. 1). Circularity (C) describes the relative sharpness of corners and edges of a particle, and roundness (R) is a measure to describe the approximation degree of the overall outline of a particle to a circle. Methods proposed by Cox [34] and Wadell [35] (Eq. 1) are used to measure the circularity and roundness of a particle, respectively. The entire morphology of a sample is represented by its average circularity C_a and average roundness R_a (Eq. 2).

$$C = \frac{4\pi A}{P^2}; \quad R = \frac{1}{n_c} \sum_{r=1}^{n_c} \frac{D_r}{D_i} \quad (1)$$

$$C_a = \frac{1}{n_p} \sum_{i=1}^{n_p} C_i; \quad R_a = \frac{1}{n_p} \sum_{i=1}^{n_p} R_i \quad (2)$$

where A and P are the area and perimeter of a particle, respectively; n_c is the number of corners of a particle; D_r and D_i are the diameters of curvature of a corner and the largest inscribed circle, respectively; n_p is the number of particles for a given sample. For a circular particle, both C and R are equal to 1. For a triangular particle, C and R are identical to 0.605 and 0, respectively.

2.2 Discrete element method and fabric evolution

A series of 2D DEM-based biaxial test simulations on samples with different PSDs, morphologies are first carried out to create training and testing datasets. For a given combination of PSD and morphology, loose and dense samples are generated. All particles are generated within a plain bounded by rigid walls. Velocity-

controlled loading is assigned vertically and constant pressure is applied laterally. The particles in DEM are assumed to be rigid without deformation, and the dynamic modelling process is controlled by time step. The deformation of particles is simulated by overlapping, and the corresponding contact force is calculated using the contact model [29]. A linear elastic contact model with Coulomb's friction criterion is applied, in which the contact force F_c is resolved into linear F^l and dashpot force F^d , and the contact moment is 0. Linear elastic and frictional inter-particle behaviours are considered. The motion of the particle is updated using Newton's second law. A typical set of variables used in DEM is summarized in Table 1.

By analysing the distribution of contacts $E(\theta)$ along with loading, which defines the portion of contacts falling within a given angular interval, fabric evolution can be inferred [36]. A second Fourier component provides a basis of approximating the distribution of contact normal orientation (Eq. 3).

$$E(\theta) = \frac{1}{2\pi} [1 + a \cos 2(\theta - \theta_a)] \quad (3)$$

where a describes the magnitude of anisotropy in the contact normal orientation and θ_a describes the direction angle of anisotropy, which can be computed using:

$$\int_0^{2\pi} E(\theta) \cos 2\theta d\theta = (a/2) \cos 2\theta_a; \quad \int_0^{2\pi} E(\theta) \sin 2\theta d\theta = (a/2) \sin 2\theta_a \quad (4)$$

Particularly, for the fabrics of normal and tangential forces, a can be replaced by a_n and a_s , respectively, meanwhile θ_a can be replaced by θ_n and θ_s , respectively. The analytical calculations of fabric anisotropy for normal force f_n and tangential force f_s can be derived from [36]:

$$f_n(\theta) = f_0 [1 + a_n \cos 2(\theta - \theta_n)]; \quad f_s(\theta) = -f_0 a_s \sin 2(\theta - \theta_s) \quad (5)$$

where f_0 is the average normal force. Noticed that Eq. 5 can also be used to describe the distribution of normal contact, in which f_0 denotes the average number of normal contacts.

2.3 Convolutional neural network

Inspired by the characteristics of CNN, two-dimensional CNN (con2d) is used to identify the particle information of granular materials. CNN generally consists of convolutional, pooling and fully-connected layers (Fig. 2). Given an image with the size of h^r (height) \times w^r (width) \times c^r (channel, 1 for grayscale image and 3 for colour image), the size is rescaled to $h^c \times w^c \times c^c \times n^c$ after convolved by n kernels [37]. The size of each kernel is identical with both height and width of f . The kernel scans the image from left to right and from top to bottom with a fixed stride s to extract features. This process is achieved by computing the dot product between the entries of the kernel and the input image, and a 2-dimensional feature map is computed subsequently. Noticed that the kernel may exceed the boundary of an image when scanning the edge. Under that condition, the pixel value of the overflow part is assigned as 0. Therefore, the size of feature maps is:

$$S_i^c = \left\lceil \frac{S_i^r}{s} \right\rceil, \quad i = h, w \quad (6)$$

where S_i^r and S_i^c denote the size of images along the i th dimension in the input and convolutional layers, respectively; $\lceil \cdot \rceil$ is the ceiling function, which maps x to the least integer larger than or equal to x .

The pooling layer merges similar features in the feature map and further reduces the size of feature map to $h^p \times w^p \times c^p \times n^c$ using Eq. 6. The Max-pooling layer is used in this study, in which the maximum value in a region of feature map represented by a filter is retained. The feature map with two dimensions is flattened finally so that they can be fed into the fully-connected layer.

2.4 Bidirectional long short-term memory neural network

BiLSTM is adopted to capture the mechanical behaviours and induced fabric evolutions of granular materials in this study. Long short-term memory (LSTM) that can store and learn historical information has been proved to be suitable for modelling path-dependent behaviours of granular materials [22]. A memory

1 cell with an entity termed as “gate” is devised and embedded into the topology of LSTM to overcome the
2
3 issues such as gradient vanishing and exploding [38] in conventional recurrent neural networks [39]. A
4
5 series of variants motivated by the “gate” mechanism has been proposed and applied to specific issues, such
6
7 as bidirectional LSTM (BiLSTM) [40] and gated recurrent unit (GRU) [41]. Herein, BiLSTM has the same
8
9 architecture of memory cell with LSTM, but BiLSTM takes use of both positive and reverse sequential
10
11 information, enhancing the interaction of sequential datasets. The number of weights and biases in BiLSTM
12
13 increases two times in comparison with LSTM. Compared with general issues in the ML domains, the
14
15 number of datasets and feature used in constitutive modelling of granular materials is much less, thereby
16
17 the BiLSTM-based constitutive model can be controlled with a simple framework. The effect of the
18
19 increasing number of weights and biases on computational efficiency is not discernible. To this end,
20
21 BiLSTM is finally employed to simulate macroscopic behaviours of granular materials in this study (Fig.
22
23 3).

3. DL-based modelling strategy and generation of datasets

3.1 Data source

41 The dataset of biaxial tests used in this study are generated using DEM (download via:
42 https://www.researchgate.net/publication/349532612_DEM_data_for_biaxial_simulations), since the simulation
43
44 results are not interfered by experimental errors, which ensures to fairly evaluate the feasibility and
45
46 performance of the DL-based modelling strategy from micro to macro scales. The height and width of the
47
48 representative volume element (RVE) are 4 and 8 mm, respectively (Fig. 4). The RVE is initially
49
50 compressed to an isotropic stress of 200 kPa, followed by the imposed velocity-controlled loading until the
51
52 vertical strain reaches 15%. Meanwhile, the lateral stress maintains constant. The trajectory of mean stress
53
54 p , deviatoric stress q , void ratio e (Eq. 7) and fabric anisotropy is recorded. The detailed modelling cases
55
56
57
58
59
60
61
62
63
64
65

1 through DEM is summarized in Table 2.

2
3
4 Herein, the preparation of loose and dense DEM samples refers to Muir and Maeda [42], in which the
5
6 maximum and minimum void ratios (e_{\max} and e_{\min}) for a sample are first calculated, and the porosity n with
7
8 a given D_r can be inferred subsequently using Eq. 8. The dense and loose samples are prepared using
9
10 frictionless particles and particles with the friction coefficient of 0.5, respectively.
11
12
13
14

$$15 \quad p = \frac{\sigma_{11} + \sigma_{22}}{2}; \quad q = \sigma_{11} - \sigma_{22}; \quad e = \frac{V_v}{V_s} \quad (7)$$

$$16 \quad n = \frac{e_{\max} - D_r (e_{\max} - e_{\min})}{1 + e_{\max} - D_r (e_{\max} - e_{\min})} \quad (8)$$

17
18
19
20
21
22
23
24
25 where σ_{11} and σ_{22} are the vertical and lateral stress, respectively; V_v and V_s are the volume of void and solid
26
27 assembly, respectively.
28
29
30

31
32 In total, 200 DEM-based biaxial tests are ultimately implemented, which sufficiently guarantees the
33
34 stability of model performance in the presence of small data regime [43]. The images of all samples, PSD,
35
36 particle morphology, stress-strain curves and induced fabric evolutions are collected to create a database.
37
38 Note that the global behaviours from numerical biaxial tests are used for datasets, although there are shear
39
40 bands inside of samples which may influence the sense of representative element of volume.
41
42
43
44
45

46 **3.2 Data preprocessing**

47
48
49 Data augmentation is employed to enlarge image database to improve the generalization ability of the CNN-
50
51 based model [44]. The application of data augmentation techniques is required to retain the original
52
53 information of samples. To this end, only flip data augmentation technique is used in this study, i.e., all
54
55 original images are flipped horizontally and vertically, thereby the size of database enlarges three times
56
57
58
59
60
61 with a total of 600 images. Each image is labelled by the PSD and sample type.
62
63
64
65

1 The raw simulated results of DEM fluctuate dramatically. Such variable datasets impose difficulties
2
3 on BiLSTM to learn useful information. Therefore, piecewise cubic Hermitean interpolation polynomials
4
5 method [45] and Savitzky-Golay denoising [46] methods are used to interpolate and smooth data, because
6
7 such two methods can enlarge the database and smooth data without changing the shape of raw stress-strain
8
9 curve (Fig. 4). Two databases are ultimately constructed, one is the image database including 600 images
10
11 of samples, another includes the corresponding stress-strain data.
12
13
14
15
16
17

18 Regarding the image database, the original pixel values for an image range from 0 to 255. If the
19
20 original images are directly fed to the CNN-based model, the values in the feature map would be extremely
21
22 large, which may result in difficulty in the convergence of a training process. Therefore, the RGB values
23
24 are rescaled into the range (0, 1) by multiplying 1/255 factor in this study [47]. Regarding the database of
25
26 stress-strain relationships, to eliminate the effect of scale difference of input parameters on the training
27
28 process of BiLSTM, all datasets are normalized into the range of (-1, 1) using the Min-Max scaling method.
29
30
31
32
33
34
35

36 Herein, 80% of images (480) are randomly selected to train the CNN-based model and the remaining
37
38 20% of images (120) are used to test the model. Because each image is flipped horizontally and vertically
39
40 at the image augmentation phase, three images present the same sample. The testing set is thus constrained
41
42 with 40 different samples for fairly evaluating the performance of the CNN-based model. Meanwhile, the
43
44 corresponding 80% (160 cases) and 20% (40 cases) of strain-stress datasets are employed to train and test
45
46 the BiLSTM-based model, respectively. It should be noted that the cases used for the training and testing
47
48 sets in the CNN and BiLSTM-based models are the same. Therefore, for a single case in the testing set, the
49
50 outputs of the CNN-based model can be directly fed to the BiLSTM-based model. The consistency of
51
52 applying the proposed DL-based modelling framework is guaranteed in this way.
53
54
55
56
57
58
59
60
61
62
63
64
65

3.3 Framework of modelling strategy

3.3.1 CNN-based particle identification model

Fig. 5 presents the schematic view of the proposed DL-based modelling framework from particle to sample scales. The modelling starts from identifying PSD and morphology of samples using CNN. By importing the image of a sample into the CNN-based model, and the corresponding PSD and morphology can be predicted. Accordingly, two CNN-based models are developed, one for PSD identification and another for particle morphology.

Motivated by Buscombe [48], to obtain the PSD of a sample, CNN is designed to identify the diameter through which 1%, 5%, 10%, 20%, 30%, 40%, 50%, 60%, 70%, 80%, 90% and 100% of particles pass. The dimension of the output in the CNN-based model is thus identical to 12. To identify particle morphology, the direct intention is to identify the ratio of each type of particles, thereby the aforementioned C_a and R_a can be calculated. However, this study merely considers round and triangular particles, and five types of samples with different mixture ratios are prescribed. Therefore, the identification of particle morphology can be converted into a classification issue, i.e., the identification of sample type. The mathematic expression for computing PSD and morphology via CNN is given in the Appendix A1.

3.3.2 BiLSTM-based mechanical prediction model

The second phase of the proposed framework is to develop a BiLSTM-based model for predicting mechanical behaviours and induced fabric evolutions of granular materials. The selection of features determines what factors can be considered by the data-driven model, thereby it is related to the application scopes of the BiLSTM-based model [49]. To this end, features are required to involve inherent properties of the studied object, state parameters and history information of stress or strain, presented as follows:

- The inherent properties of granular materials are identified by the CNN-based model at the first phase. Herein, the mean particle size d_{50} and the coefficient of uniformity C_u derived from the PSD as representative indicators are selected as the input variables. The inherent properties of a sample are thus represented by four variables, i.e. d_{50} , C_u , C_a and R_a .
- State variables are employed to reproduce the experimental process including initial void ratio e_0 , relative density D_r and vertical strain ε .
- The outputs of the BiLSTM-based model at previous time steps are fed to the input variables for considering history loading path.

Hence, the input parameters of the BiLSTM-based model for modelling mechanical behaviours are $\mathbf{x} = [p, q, e, \varepsilon, e_0, D_r, d_{50}, C_u, C_a, R_a]$, and $\mathbf{x} = [a, a_n, a_s, \varepsilon, e_0, D_r, d_{50}, C_u, C_a, R_a]$ for predicting fabric evolutions.

The direction angle of fabric anisotropy roughly maintains constant in the biaxial test, thereby anisotropy variables regarding the magnitude of anisotropy a, a_n, a_s are predicted while the direction angle of anisotropy maintains initial values. The detailed mathematic expression of a BiLSTM-based model is introduced in the Appendix A2.

4. Applications

4.1 Training of the CNN-based model

The development of the DL-based model is implemented using Keras with the Tensorflow backend [50]. The training of CNN is first to determine the number of convolutional, pooling, fully-connected layers, and the hidden neurons in each layer. Other hyper-parameters such as optimizer, learning rate, activation function, batch size and epochs are required to be finely tuned. The prediction of PSD is a regression issue, mean square error (MSE) is thus set as the loss function. Meanwhile, k -fold cross-validation method is

employed to detect the overfitting issue. The loss function is finally formulated using:

$$\text{MSE} = \frac{1}{k} \frac{1}{n_{sub}} \sum_{i=1}^{n_{sub}} (y_i^p - y_i^a)^2 \quad (9)$$

where n_{sub} is the number of datasets in a sub validation set; k is the number of folds, which is usually set as 10; y_i^p and y_i^a are predicted and actual values, respectively. The configurations of the CNN-based model are determined using the trial-and-error method, and the detailed process is not presented for brevity. The final configurations are summarized in Table 3. The number of weights and biases are 6193176 and 92, respectively. It can be seen from Fig. 6a that MSE values on the training and testing sets are small and rapidly converge within 50 epochs.

The shallow layers of the CNN-based model focus on extracting features of each sample, while the deep layers are used to fuse features and the outputs tend to be abstract. To reveal the mechanism of the CNN-based model to identify the PSD, the outputs at the shallow layers are illustrated. Feature maps in the fundamental four layers of the model are illustrated in Fig. 7. When a particle is convolved by a kernel, the output is dependent on its size. After three kernels convolve the whole image (con2d_1, con2d_2, con2d_3) and pass through the pooling layer (max_pooling2d_1), particle size information is stored in the feature map with different values and are thus marked with different colours. Accordingly, the CNN-based model can distinguish the particle size and predict PSD.

The identification of particle morphology is a classification issue, thereby the average cross-entropy (ACE) is tailored for objectively calculating the discrimination between predicted and actual labels [51].

$$\text{ACE} = -\frac{1}{n} \sum_{i=1}^n \sum_{j=1}^C y_{j,i}^a \ln f_j(x_i) \quad (10)$$

where C is the number of classification labels; n is the total number of datasets; $y_{j,i}^a$ is the actual label; $f_j(x_i)$

1 is the output of the CNN-based model for an input x_i . The evolution of ACE values on the training and
2
3 testing sets is presented in Fig. 6b. The number of weights and biases are 6190072 and 61, respectively.
4
5
6 The training process rapidly maintains stable, and the ACE value accordingly decreases to 0 within 50
7
8 epochs. Similar to the identification of particle size, the pixel size and value for a triangular particle and a
9
10 circular one are different, thereby CNN can extract the particle morphology information. The process of
11
12 extracting features in the CNN-based particle morphology identification model is the same as the principle
13
14 revealed in Fig. 7, the feature map in each layer is thus not presented for brevity.
15
16
17
18
19
20

21 **4.2 Training of the BiLSTM-based model**

22
23
24 Similar to CNN, the training of the BiLSTM-based model is primarily to determine the number of hidden
25
26 layers and hidden neurons in each layer, and other hyper-parameters are required to be finely tuned. The
27
28 configurations of the BiLSTM-based model are determined using the trial-and-error method, and the results
29
30 are presented in Table 3. The number of weights and biases are 67560 and 963, respectively.
31
32
33
34
35

36 One of the important configurations in BiLSTM is the time step, which determines how long the stress-
37
38 strain history can be taken into account by the BiLSTM-based model. The history information enforces the
39
40 capacity of modelling mechanical behaviours, but too long history information also degrades the learning
41
42 efficiency and causes overfitting. To this end, three steps of stress-strain history before the current step are
43
44 selected, i.e., the time step of BiLSTM is set as 3. Because the number of datasets at each experiment is
45
46 identical to 1503, the batch size is thus set as 1503 to ensure BiLSTM can learn the entire information of
47
48 an entire experiment at each round. Considering the prediction of mechanical behaviours is a regression
49
50 issue, the MSE is also set as the loss function. The evolution of MSE values generated by the BiLSTM-
51
52 based models for predicting mechanical responses and induced fabric evolutions during the training process
53
54 is presented in Figs. 6c and 6d, respectively. The MSE values on both training and testing sets dramatically
55
56
57
58
59
60
61
62
63
64
65

1 decrease to a negligible value within 50 epochs. Compared with the evolution of MSE values generated by
 2
 3 the CNN-based PSD identification model (Fig. 6a), the MSE values generated by the BiLSTM-based
 4
 5 models are more fluctuant, because the ranges of outputs in the BiLSTM-based model is much larger than
 6
 7 the range of outputs (i.e. diameters of particles) in the CNN-based PSD identification model. Overall, the
 8
 9 MSE values are small, thereby the performance of training can be guaranteed.
 10
 11
 12
 13
 14

15 **4.3 Modelling results of the CNN-based model**

16
 17
 18 After the optimum configurations of the CNN-based model are determined, the training and testing sets are
 19
 20 fed to the model to examine its generalization ability. To quantitatively evaluate the performance of the
 21
 22 BiLSTM-based model. Absolute and relative error indicators, i.e., mean absolute error (MAE) and mean
 23
 24 absolute percentage error (MAPE), are computed.
 25
 26
 27
 28
 29
 30

$$31 \quad \text{MAE} = \frac{1}{n} \sum_{i=1}^n |y_i^p - y_i^a|; \quad \text{MAPE} = \frac{1}{n} \sum_{i=1}^n \left| \frac{y_i^p - y_i^a}{y_i^a} \right| \times 100\% \quad (11)$$

32
 33
 34
 35 The MAE and MAPE values generated by the CNN-based model for predicting PSD is summarized
 36
 37 in Table 4. The error is not discernible and MAPE value is largely owing to the small value of the
 38
 39 denominator. To comprehensively evaluate model performance, the predicted results of 5 samples in the
 40
 41 testing set with different mixture ratio and PSD are particularly selected. It can be seen from Fig. 8 that the
 42
 43 predicted PSD curves are close to the evolution of actual points, and the calculated d_{50} and C_u are roughly
 44
 45 identical to the actual results. Such factors indicate CNN deduces plausible identification for the PSD of
 46
 47 granular materials.
 48
 49
 50
 51
 52
 53
 54
 55

56 The result of identifying particle morphology on the testing set is presented in Fig. 9. The confusion
 57
 58 matrix is used to evaluate the classification accuracy of the CNN-based particle morphology identification
 59
 60 model. The sum of probability at each column is identical to 0. Given an actual mixture ratio, the predicted
 61
 62
 63
 64
 65

1 mixture ratio has five conditions, but only one condition that is located at the diagonal line is correct. It can
2
3 be observed that the CNN-based model perfectly identifies the mixture ratio with the probability along the
4
5 diagonal line of 1. CNN provides a direct and reliable way of identifying the particle information of granular
6
7
8 materials.
9

10 11 **4.4 Modelling results of the BiLSTM-based model**

12
13
14
15 The number of datasets used in the BiLSTM-based model is large. Each simulation test consists of 1503
16
17 datasets, and the training and testing sets include 160 and 40 numerical simulations, respectively. Although
18
19
20 MAE and MAPE values on the testing set are roughly 5 times the values on the training set, the prediction
21
22 errors are negligible (Table 4). To reveal the modelling results of the BiLSTM-based model, the mechanical
23
24 behaviours of 5 samples in the testing set (the same as the selected samples in the former section) are
25
26
27 illustrated (Fig. 10). The BiLSTM-based model can accurately capture the relationships of p - ε , q - ε and e -
28
29
30 ε . Cho et al. [52] demonstrated that the increasing angularity leads to the increasing strength of soil mass,
31
32
33 extreme e_{\max} and e_{\min} . The simulated results in Fig. 10 also present a similar trend, in which the increasing
34
35 ratio of triangular particles results in higher peak stress and lower initial void ratio. The BiLSTM-based
36
37
38 model captures the effects of mixture ratio of on the mechanical behaviours. For a biaxial test simulated
39
40
41 using DEM, a 2-dimensional granular specimen dilates at a greater rate than the real specimen particularly
42
43
44 for angular particle [53, 54]. Moreover, the increasing triangular particles cause denser sample with a
45
46
47 smaller initial void ratio, and the volumetric dilatancy is more obvious due to the rolling of triangular
48
49
50 particles during the shearing process. Therefore, it can be seen from Fig. 10 that the volumetric compression
51
52
53 on the loose sample merely appears as the ratio of triangular particles is less than 75%. Volumetric dilatancy
54
55
56 is observed on both dense and loose samples in most of cases. Mechanical behaviours including stress
57
58
59 softening and volumetric dilatancy on the dense samples, stress hardening and volumetric compression on
60
61
62
63
64
65

1 the loose samples with a large ratio of circular particles can accurately be captured by the BiLSTM-based
2
3 model. Such factors indicate BiLSTM understands the intrinsic physical mechanism of granular materials,
4
5
6 showing great potential of modelling their mechanical behaviours.
7

8
9 The prediction errors on the induced fabric evolutions are also small (Table 4). MAE and MAPE values
10
11 on the testing set double the values on the training set. Fig. 11 presents the evolution of predicted and
12
13 measured a , a_n and a_s , which reveals the magnitude of anisotropy of contact number, contact normal force
14
15 and tangential force, respectively. The BiLSTM-based model is capable of accurately predicting the
16
17 evolution of induced anisotropy. With the increasing ratio of triangular particles, the magnitude of
18
19 anisotropy increases. Detailed inspection of the modelling results indicates that the peak values of a , a_n and
20
21 a_s reach at ε of around 2%, which is close to the position where peak strength reaches (Fig. 10). Thereafter
22
23 the values of a , a_n and a_s reduces for the dense samples, and maintains steadily for the loose samples. The
24
25 ultimate values of a , a_n and a_s of dense and loose samples with the same mixture ratio are roughly identical.
26
27 Such results reflect the variation of the microstructure of granular samples, and it further induces the
28
29 corresponding responses of global mechanical behaviours. Overall, BiLSTM is capable of identifying the
30
31 physical phenomena on both microscopic and macroscopic scales.
32
33
34
35
36
37
38
39
40
41
42
43
44

45 **5. Evaluation of generalization ability and robustness**

46
47 Understanding the performance of DL-based model on unknown data is vitally important to guarantee its
48
49 application scope. Four additional numerical biaxial tests with two mixture ratios (R10_T90 and R90_T10)
50
51 that out of the range of the training set are conducted using DEM, in which the d_{50} and C_u of the R10_T90
52
53 sample are 0.0006 and 3.5, respectively. The d_{50} and C_u of the R90_T10 sample are 0.0007 and 3.75,
54
55 respectively. Both dense and loose samples for each mixture ratio are prepared for testing set. For testing,
56
57 the images of the four new samples as inputs are fed to the developed CNN-based model to predict the PSD,
58
59
60
61
62
63
64
65

1 i.e., d_{50} and C_u . They are then automatically fed to the developed BiLSTM-based model with pre-assigned
2
3 morphology information to predict the mechanical behaviours of these new samples. The predicted results
4
5 are compared with simulated results of DEM to evaluate the generalization ability and robustness of the
6
7 proposed DL-based modelling framework. Good agreement demonstrates that the DL-based model can still
8
9 accurately capture the evolution of mechanical responses and induced fabric evolution for samples with
10
11 novel particle morphology. Based on the predicted a , a_n and a_s , the distribution of contact normal can be
12
13 fitted using Eq. 5. The results for a dense sample R10_T90 as a representative example are illustrated in
14
15 Fig. 13. It can be observed that the fitted contact normal distribution, distributions of normal and tangential
16
17 forces show excellent agreement with the measured results. The evolution of anisotropy with the increasing
18
19 vertical strain can be accurately captured. These factors indicate the proposed DL-based modelling
20
21 framework is promising for multiscale modelling. The DL-based model is capable of accurately capturing
22
23 the effects of particle information on the mechanical behaviours and induced anisotropy, such as effects of
24
25 particle morphology and relative density on the characteristics of deformation and strength with the
26
27 magnitude of anisotropy.
28
29
30
31
32
33
34
35
36
37
38
39
40
41
42
43
44

45 **6. Conclusions**

46
47 A DL-based modelling strategy from image of particles to global behaviours of the sample of granular
48
49 materials has been developed. In this approach, CNN was first used to extract the particle information (PSD
50
51 and morphology), and BiLSTM neural network was then employed to simulate the global mechanical
52
53 behaviours and fabric evolutions of granular materials. The datasets of biaxial samples and tests were
54
55 created using DEM with different particle information for training and testing.
56
57
58
59
60
61
62

63 As demonstrated, the proposed CNN-based model part is capable of accurately identifying mean
64
65

1 diameter and coefficient of uniformity of a granular sample, as well as circularity and roundness of a particle,
2
3 which provides a direct and easy way of acquiring the particle information of granular materials. The effects
4
5 of PSD, particle morphology and relative density on the global mechanical behaviours and induced fabric
6
7 evolutions of granular materials have been well captured by the BiLSTM-based model with the particle
8
9 information as connecting parameters. Thus, the feasibility and reliability of the proposed modelling
10
11 strategy have been evaluated.
12
13
14
15

16
17
18 It should be pointed out once two DL-based model parts embedded in the proposed modelling
19
20 framework are well trained, the whole modelling process from extraction of particle information to
21
22 prediction of mechanical and fabric behaviours can be completed within seconds. The computational source
23
24 is dramatically saved. Moreover, the proposed modelling framework is genetic, which means the datasets
25
26 can be replaced by the real experimental or brilliant numerical datasets to investigate different issues, such
27
28 as Micro-CT for real granular materials on real granular materials, 3D numerical modelling and making
29
30 use of contact distribution to consider the fabric of materials. Meanwhile, the applied DL algorithms can
31
32 also be updated by more advanced and effective algorithms considering the rapid development in the DL
33
34 domain.
35
36
37
38
39
40
41
42
43
44
45
46
47

48 **Appendix**

49 **A1 - Mathematic expression of the CNN-based model**

50
51
52 Given a set of images of a soil sample that are digitalized by \mathbf{x} , the computation of the CNN-based model
53
54 with two convolutional layers, one pooling layer and one fully-connected layer as a representative example
55
56 is carried out.
57
58
59
60
61
62
63
64
65

(1) from the input \mathbf{x} to the first convolutional \mathbf{C}^1 layers:

$$\mathbf{C}_j^1 = \text{ReLU} \left[\text{sum} \left(\mathbf{W}_{C_j^1} \odot \mathbf{x}_i \right) + b_j \right] \quad (\text{A1})$$

where \mathbf{C}_j^1 denotes the outputs convolved by the j th kernel in the C^1 layer; $\mathbf{W}_{C_j^1}$ is weights of the j th kernel in the C^1 layer; b_j is a bias term at the j th kernel; *sum* denotes the summation of all elements; ReLU represents the activation function rectified linear unit (ReLU).

(2) from the first \mathbf{C}^1 to the second \mathbf{C}^2 convolutional layers:

$$\mathbf{C}_j^2 = \text{ReLU} \left[\text{sum} \left(\mathbf{W}_{C_j^2} \odot \mathbf{C}_i^1 \right) + b_j \right] \quad (\text{A2})$$

where the meaning of all notations can refer to Eq. A1.

(3) from the second convolutional \mathbf{C}^2 to the pooling \mathbf{P}^1 layers:

$$\mathbf{P}_{i,j}^1 = \max \left(\mathbf{C}_{i,j}^2, \dots, \mathbf{C}_{i,j+f_{p^1}-1}^2, \dots, \mathbf{C}_{i+f_{p^1}-1,j}^2, \dots, \mathbf{C}_{i+f_{p^1}-1,j+f_{p^1}-1}^2 \right) \quad (\text{A3})$$

where max function indicates the output at the \mathbf{P}^1 layer is the maximum value of a region covered by a kernel with a size of f_{p^1} .

(4) from the pooling \mathbf{P}^1 to the fully-connected \mathbf{F}^1 layers:

$$\mathbf{F}^1 = \text{ReLU} \left[\mathbf{W}_{F^1} \times \left(\mathbf{P}_1^1, \dots, \mathbf{P}_2^1, \dots, \mathbf{P}_{n_{p^1}}^1 \right) + \mathbf{b}_{F^1} \right] \quad (\text{A4})$$

where n_{p^1} denotes a total of elements in the \mathbf{P}^1 layer; \mathbf{W}_{F^1} and \mathbf{b}_{F^1} are the weights and biases connecting \mathbf{P}^1 and \mathbf{F}^1 layers, respectively.

(6) from the fully-connected \mathbf{F}^1 to the output \mathbf{y} layers:

$$\mathbf{y}_{PSD} = \mathbf{W}^y \times \mathbf{F}^n + \mathbf{b}^y; \quad \mathbf{y}_{mor} = e^{\mathbf{W}^y \times \mathbf{F}^n + \mathbf{b}^y} / \sum e^{\mathbf{W}^y \times \mathbf{F}^n + \mathbf{b}^y} \quad (\text{A5})$$

where \mathbf{W}^y and \mathbf{b}^y are the weights and biases connected \mathbf{F}^1 and \mathbf{y} layers, respectively. Eqs. The computation of regression and classification problems is different, as shown in A5, where the outputs of PSD (\mathbf{y}_{PSD}) and

particle morphology (y_{mor}) identification models are given.

A2 - Mathematic expression of the BiLSTM-based model

In BiLSTM (Fig. 3), ${}^p\mathbf{W}$, ${}^p\mathbf{U}$ and ${}^p\mathbf{b}$ are the weights matrices and biases vector used for the positive data flow. ${}^r\mathbf{W}$, ${}^r\mathbf{U}$ and ${}^r\mathbf{b}$ are used for the reverse data flow. The same architecture of the memory cell is used for positive and reverse directions, which means the dimensions of matrices and biases used in both positive and reverse data flow is identical, but the values are different. The mathematical expression of the BiLSTM-based model with one LSTM layer, one fully-connected layer and a time step of t as a representative example is revealed as follows:

(1) From the first input \mathbf{x}^1 to the LSTM layers at the first time step ${}^p\mathbf{h}^1$ (positive data flow), it starts from the calculation of the forget, input and output gates:

$$\begin{aligned} {}^p\mathbf{f}^1 &= \sigma\left({}^p\mathbf{W}_f \times \mathbf{x}^1 + {}^p\mathbf{U}_f \times {}^p\mathbf{h}^0 + {}^p\mathbf{b}_f\right) \\ {}^p\mathbf{i}^1 &= \sigma\left({}^p\mathbf{W}_i \times \mathbf{x}^1 + {}^p\mathbf{U}_i \times {}^p\mathbf{h}^0 + {}^p\mathbf{b}_i\right) \\ {}^p\mathbf{o}^1 &= \sigma\left({}^p\mathbf{W}_o \times \mathbf{x}^1 + {}^p\mathbf{U}_o \times {}^p\mathbf{h}^0 + {}^p\mathbf{b}_o\right) \end{aligned} \quad (\text{A6})$$

where subscript f , i and o denote the weight matrices and bias vectors used in the forget, input and output gates, respectively. σ is the activation function *sigmoid*. Superscript p denotes the positive data flow. ${}^p\mathbf{h}^0$ with zero values denotes the initial hidden state. The output of memory cell is obtained by:

$${}^p\tilde{\mathbf{c}}^1 = \text{ELU}\left({}^p\mathbf{W}_c \times \mathbf{x}^1 + {}^p\mathbf{U}_c \times {}^p\mathbf{h}^0 + {}^p\mathbf{b}_c\right); \quad {}^p\mathbf{c}^1 = {}^p\mathbf{f}^1 \odot {}^p\mathbf{c}^0 + {}^p\mathbf{i}^1 \odot {}^p\tilde{\mathbf{c}}^1; \quad {}^p\mathbf{h}^1 = {}^p\mathbf{o}^1 \odot \text{ELU}\left({}^p\mathbf{c}^1\right) \quad (\text{A7})$$

where \odot denotes the element-wise product. ${}^p\mathbf{c}^0$ with zero values denotes the initial memory state. ELU is the activation function exponential linear unit.

(2) from the first ${}^p\mathbf{h}^1$ to the next time step ${}^p\mathbf{h}^2, {}^p\mathbf{h}^3, \dots, {}^p\mathbf{h}^t$ in the LSTM layers: the calculation is similar to

Eqs. A6-A7, the only difference is the \mathbf{x}^1 and ${}^p\mathbf{h}^0$ are replaced by \mathbf{x}^2 and ${}^p\mathbf{h}^1$, respectively. The subsequent calculation steps are similarly repeated until the ${}^p\mathbf{h}^t$ is obtained.

(3) the ultimate output of the first LSTM layer \mathbf{h}^t : procedure (1) and (2) reveal the positive data flow, and half of the first hidden state. The calculation method of reverse data flow is same, in which the only difference is that the calculation starts from the t th time, and ${}^r\mathbf{W}$, ${}^r\mathbf{U}$ and ${}^r\mathbf{b}$ are used instead of ${}^p\mathbf{W}$, ${}^p\mathbf{U}$ and ${}^p\mathbf{b}$. Therefore, the ultimate output of the first hidden layer is obtained by integrating the outputs of memory cell in both positive and reverse data flow using:

$$\mathbf{h}^1 = {}^p\mathbf{h}^1 \oplus {}^r\mathbf{h}^t \quad (\text{A8})$$

where \oplus denotes concatenation operation.

(4) from the LSTM \mathbf{h}^1 to the fully-connected layers \mathbf{F} :

$$\mathbf{F} = \tanh(\mathbf{W}_F \times \mathbf{h}^1 + \mathbf{b}_F) \quad (\text{A9})$$

where \mathbf{W}_F and \mathbf{b}_F are the weights and biases used in the fully-connected layer, respectively.

(5) from the fully-connected to the output layers:

$$\mathbf{y} = \mathbf{W}_y \times \mathbf{F} + \mathbf{b}_y \quad (\text{A10})$$

where \mathbf{W}_y and \mathbf{b}_y are the weights and biases used in the output layer, respectively. \mathbf{y} is the predicted mechanical responses or fabric evolutions based on the input \mathbf{x} .

Acknowledgement

This research was financially supported by the Research Grants Council (RGC) of Hong Kong Special Administrative Region Government (HKSARG) of China (Grant No.: 15209119, R5037-18F).

References

- [1] S. Zhao, T.M. Evans, X. Zhou, Effects of curvature-related DEM contact model on the macro- and micro-mechanical behaviours of granular soils, *Géotechnique*, 68 (2018) 1085-1098.
- [2] Y.F. Jin, Z.Y. Yin, Z.X. Wu, A. Daouadji, Numerical modeling of pile penetration in silica sands considering the effect of grain breakage, *Finite Elem. Anal. Des.*, 144 (2018) 15-29.
- [3] Z.Y. Yin, P.-Y. Hicher, C. Dano, Y.F. Jin, Modeling mechanical behavior of very coarse granular materials, *J. Eng. Mech.*, 143 (2017) C4016006.
- [4] Z.Y. Yin, J. Zhao, P.Y. Hicher, A micromechanics-based model for sand-silt mixtures, *Int. J. Solids Struct.*, 51 (2014) 1350-1363.
- [5] Y.J. Liu, G. Li, Z.Y. Yin, Christophe Dano, P.Y. Hicher, J.H. Wang, X.H. Xia, Influence of grading on undrained behavior of granular materials, *C. R. Mec.*, 342 (2014) 85-95.
- [6] J. Yang, Z.Y. Yin, F. Laouafa, P.-Y. Hicher, Analysis of suffusion in cohesionless soils with randomly distributed porosity and fines content, *Comput. Geotech.*, 111 (2019) 157-171.
- [7] H.M. Beakawi Al-Hashemi, O.S. Baghabra Al-Amoudi, A review on the angle of repose of granular materials, *Powder Technol.*, 330 (2018) 397-417.
- [8] Y.T. Feng, T. Zhao, J. Kato, W. Zhou, Towards stochastic discrete element modelling of spherical particles with surface roughness: A normal interaction law, *Comput. Meth. Appl. Mech. Eng.*, 315 (2017) 247-272.
- [9] Z. Lai, Q. Chen, L. Huang, Fourier series-based discrete element method for computational mechanics of irregular-shaped particles, *Comput. Meth. Appl. Mech. Eng.*, 362 (2020) 112873.
- [10] K. Shibata, S. Koshizuka, I. Masaie, Cost reduction of particle simulations by an ellipsoidal particle model, *Comput. Meth. Appl. Mech. Eng.*, 307 (2016) 411-450.
- [11] K. Kildashti, K. Dong, B. Samali, An accurate geometric contact force model for super-quadric particles, *Comput. Meth. Appl. Mech. Eng.*, 360 (2020) 112774.
- [12] G. Mollon, J. Zhao, 3D generation of realistic granular samples based on random fields theory and Fourier shape descriptors, *Comput. Meth. Appl. Mech. Eng.*, 279 (2014) 46-65.
- [13] L.M. Wei, J. Yang, On the role of grain shape in static liquefaction of sand-fines mixtures, *Géotechnique*, 64 (2014) 740-745.
- [14] F. Ezzein, R. Bathurst, A transparent sand for geotechnical laboratory, *Geotech. Test. J.*, 34 (2011) 590-601.
- [15] J. Chu, An experimental examination of the critical state and other similar concepts for granular soils, *Can. Geotech. J.*, 32 (1995) 1065-1075.
- [16] H.L. Wang, Y.J. Cui, F. Lamas Lopez, N. Calon, G. Saussine, J.C. Dupla, J. Canou, P. Aïmediou, R.P. Chen, Investigation on the mechanical behavior of track-bed materials at various contents of coarse grains, *Constr. Build. Mater.*, 164 (2018) 228-237.
- [17] T. Ueda, T. Matsushima, Y. Yamada, DEM simulation on the one-dimensional compression behavior of various shaped crushable granular materials, *Granul. Matter*, 15 (2013) 675-684.
- [18] P. Zhang, Z.Y. Yin, Y.F. Jin, T. Chan, F.P. Gao, Intelligent modelling of clay compressibility using hybrid meta-heuristic and machine learning algorithms, *Geosci. Front.*, 12 (2021) 441-452.
- [19] P. Zhang, Z.Y. Yin, Y.F. Jin, T.H.T. Chan, A novel hybrid surrogate intelligent model for creep index prediction based on particle swarm optimization and random forest, *Eng. Geol.*, 265 (2020) 105328.

- [20] J. Tian, C. Qi, Y. Sun, Z.M. Yaseen, Surrogate permeability modelling of low-permeable rocks using convolutional neural networks, *Comput. Meth. Appl. Mech. Eng.*, 366 (2020) 113103.
- [21] M. Schwarzer, B. Rogan, Y. Ruan, Z. Song, D.Y. Lee, A.G. Percus, V.T. Chau, B.A. Moore, E. Rougier, H.S. Viswanathan, G. Srinivasan, Learning to fail: Predicting fracture evolution in brittle material models using recurrent graph convolutional neural networks, *Comput. Mater. Sci.*, 162 (2019) 322-332.
- [22] P. Zhang, Z.Y. Yin, Y.F. Jin, G.L. Ye, An AI-based model for describing cyclic characteristics of granular materials, *Int. J. Numer. Anal. Methods Geomech.*, 44 (2020) 1315-1335.
- [23] K. Wang, W. Sun, Meta-modeling game for deriving theory-consistent, microstructure-based traction–separation laws via deep reinforcement learning, *Comput. Meth. Appl. Mech. Eng.*, 346 (2019) 216-241.
- [24] P. Zhang, Z.Y. Yin, Y.F. Jin, State-of-the-art review of machine learning applications in constitutive modeling of soils, *Arch. Comput. Method Eng.*, (2021).
- [25] J. Fonseca, C. O'Sullivan, M.R. Coop, P.D. Lee, Quantifying the evolution of soil fabric during shearing using scalar parameters, *Géotechnique*, 63 (2013) 818-829.
- [26] J. Fonseca, W.W. Sim, T. Shire, C. O'Sullivan, Microstructural analysis of sands with varying degrees of internal stability, *Géotechnique*, 64 (2014) 405-411.
- [27] S. Nadimi, J. Fonseca, A micro finite-element model for soil behaviour, *Géotechnique*, 68 (2018) 290-302.
- [28] T. Zhao, F. Dai, N.W. Xu, Y. Liu, Y. Xu, A composite particle model for non-spherical particles in DEM simulations, *Granul. Matter*, 17 (2015) 763-774.
- [29] P.A. Cundall, O.D.L. Strack, A discrete numerical model for granular assemblies, *Géotechnique*, 29 (1979) 47-65.
- [30] N.T. Ngo, B. Indraratna, C. Rujikiatkamjorn, Micromechanics-based investigation of fouled ballast using large-scale triaxial tests and discrete element modeling, *J. Geotech. Geoenviron. Eng.*, 143 (2017) 04016089.
- [31] M.O. Ciantia, M. Arroyo, F. Calvetti, A. Gens, An approach to enhance efficiency of DEM modelling of soils with crushable grains, *Géotechnique*, 65 (2015) 91-110.
- [32] J.M. Harmon, D. Arthur, J.E. Andrade, Level set splitting in DEM for modeling breakage mechanics, *Comput. Meth. Appl. Mech. Eng.*, 365 (2020) 112961.
- [33] D. Reimann, K. Nidadavolu, H. ul Hassan, N. Vajragupta, T. Glasmachers, P. Junker, A. Hartmaier, Modeling macroscopic material behavior with machine learning algorithms trained by micromechanical simulations, *Front. Mater.*, 6 (2019) 1-19.
- [34] E.A. Cox, A method for assigning numerical and percentage values to the degree of roundness of sand grains, *J. Paleontol.*, 1 (1927) 179-183.
- [35] H. Wadell, Volume, shape, and roundness of rock particles, *J. Paleontol.*, 40 (1932) 443-451.
- [36] L. Rothenburg, R.J. Bathurst, Analytical study of induced anisotropy granular materials, *Géotechnique*, 39 (1989) 601-614.
- [37] Z. Zhong, T.R. Carr, X.M. Wu, G. Wang, Application of a convolutional neural network in permeability prediction: A case study in the Jacksonburg-Stringtown oil field, West Virginia, USA, *Geophysics*, 84 (2019) 363-373.
- [38] Y. LeCun, Y. Bengio, G. Hinton, Deep learning, *Nature*, 521 (2015) 436-444.
- [39] S. Hochreiter, J. Schmidhuber, Long short-term memory, *Neural Comput.*, 9 (1997) 1735–1780.
- [40] A. Graves, J. Schmidhuber, Framewise phoneme classification with bidirectional LSTM and other neural network architectures, *Neural Netw.*, 18 (2005) 602-610.
- [41] K. Cho, B. Van Merriënboer, C. Gulcehre, v. Bahdanau, F. Bougares, H. Schwenk, Y. Bengio, Learning

- phrase representations using RNN Encoder–Decoder for statistical machine translation, arXiv:1406.1078v3, (2014).
- [42] W. Muir, David, K. Maeda, Changing grading of soil: effect on critical states, *Acta Geotech.*, 3 (2007) 3-14.
- [43] C. Grigo, P.-S. Koutsourelakis, A physics-aware, probabilistic machine learning framework for coarse-graining high-dimensional systems in the Small Data regime, *J. Comput. Phys.*, 397 (2019) 108842.
- [44] A. Krizhevsky, I. Sutskever, G. Hinton, ImageNet classification with deep convolutional neural networks, in: *NIPS*, 2012.
- [45] C.B. Moler, *Numerical computing with MATLAB*, SIAM, 2004.
- [46] A. Savitzky, M.J.E. Golay, Smoothing and differentiation of data by simplified least squares procedures, *Anal. Chem.*, 36 (1964) 1627-1639.
- [47] S. Joshi, S. Saxena, N. Khanna, First steps toward CNN based source classification of document images shared over messaging app, *Signal Process. Image Commun.*, 78 (2019) 32-41.
- [48] D. Buscombe, SediNet: a configurable deep learning model for mixed qualitative and quantitative optical granulometry, *Earth Surf. Proc. Land.*, 45 (2020) 638-651.
- [49] P. Zhang, R.P. Chen, H.N. Wu, Real-time analysis and regulation of EPB shield steering using Random Forest, *Automat. Constr.*, 106 (2019) 102860.
- [50] F. Chollet, Keras, <https://github.com/keras-team/keras>, (2015).
- [51] J. Ye, Single valued neutrosophic cross-entropy for multicriteria decision making problems, *Appl. Math. Model.*, 38 (2014) 1170-1175.
- [52] G.C. Cho, J. Dodds, J.C. Santamarina, Particle shape effects on packing density, stiffness, and strength: natural and crushed sands, *J. Geotech. Geoenviron. Eng.*, 132 (2006) 591-602.
- [53] Rothenburg L, B.R. J., Micromechanical features of granular assemblies with planar elliptical particles, *Géotechnique*, 42 (1992) 79-95.
- [54] X.Y. Jing, W.H. Zhou, H.X. Zhu, Z.Y. Yin, Y.M. Li, Analysis of soil-structural interface behavior using three-dimensional DEM simulations, *Int. J. Numer. Anal. Methods Geomech.*, 42 (2018) 339-357.

Table

Table 1 Parameters used in DEM modelling

Parameter	Value
Particle density (kg/m ³)	2650
Inter-particle friction coefficient	0.5
Friction coefficient of particle-wall	0
Inter-particle contact normal stiffness (N/m)	1.5×10 ⁸
Inter-particle contact shear stiffness (N/m)	1.0×10 ⁸
Normal stiffness of particle-wall (N/m)	15×10 ⁸
Shear stiffness of particle-wall (N/m)	10×10 ⁸
Damping ratio	0.7

Table 2 Summary of numerical sample types for the database

5 Mixture ratios	R0_T100 (100% triangle particles), R25_T75 (25% round and 75% triangle particles), R50_T50 (50% round and 50% triangle particles), R75_T25 (75% round and 25% triangle particles), R100_T0 (100% round particles)
20 PSDs (d_{50} /mm, C_u) for each mixture ratio	(0.55, 1.83), (0.7, 3.75), (0.8, 5), (0.6, 3.5), (0.4, 1.6), (0.55, 3), (0.9, 5), (0.6, 3.5), (0.6, 3.5), (0.5, 1.83), (0.55, 2.75), (0.7, 3.75), (0.8, 4.5), (0.6, 3.5), (0.4, 1.6), (0.55, 3), (0.6, 3.5), (1.2, 6.5), (0.6, 3.5), (0.5, 1.83)
2 D_r (%) for each mixture ratio	10, 80
Total number of simulation cases	5×20×2 = 400

Table 3 Configurations of the DL-based model

Model type	Layer type	Num. of neurons	Num. of kernel	kernel size	Activation function	kernel initializer	Note
PSD	C	/	8	3, 3	<i>ReLU</i>	RU	optimizer = SGD with learning rate of 1e-4, decay of 1e-6 and momentum of 0.9; loss function = MSE; batch size = 1
	C	/	8	3, 3	<i>ReLU</i>	RU	
	C	/	16	3, 3	<i>ReLU</i>	RU	
	P	/	/	2, 2	/	/	
	C	/	16	3, 3	<i>ReLU</i>	RU	
	P	/	/	2, 2	<i>ReLU</i>	/	
Particle morphology	F	32	/	/	<i>ReLU</i>	GU	optimizer = SGD with learning rate of 1e-4, decay of 1e-6 and momentum of 0.9; loss function = ACE; batch size = 1
	F (output)	12	/	/	<i>linear</i>	GU	
	C	/	8	3, 3	<i>ReLU</i>	RU	
	P	/	/	2, 2	/	/	
	C	/	16	3, 3	<i>ReLU</i>	RU	
Mechanical behaviours/ Fabric evolutions	P	/	/	2, 2	/	/	optimizer = <i>Adam</i> loss function = MSE; batch size = 1503
	F	32	/	/	<i>ReLU</i>	GU	
	F (output)	5	/	/	<i>softmax</i>	GU	
	B	60	/	/	<i>ELU</i>	GU	
	B	60	/	/	<i>ELU</i>	GU	
	F (output)	3	/	/	<i>linear</i>	GU	

Note: C, P, F, B = convolutional, pooling, fully-connected and BiLSTM layer; RU = random uniform; GU = glorot uniform; SGD = stochastic gradient descent

Table 4 Values of indicators generated by DL based model

Model type	Training set		Testing set	
	MAE	MAPE	MAE	MAPE
PSD	1.0E-4 mm	15.82%	1.3E-4 mm	21.35%
Mechanical responses	0.2 kPa	0.17%	1.1 kPa	0.64%
Fabric evolutions	4.1E-5	0.34%	1.1E-4	0.89%

Figure caption

Fig. 1 Definition of particle circularity and roundness

Fig. 2 Schematic view of CNN

Fig. 3 Schematic view of BiLSTM

Fig. 4 A representative numerical biaxial test for 2D granular assembly and modelling results

Fig. 5 Flowchart of the proposed DL-based modelling framework

Fig. 6 Evolution of loss value: (a) CNN-based PSD identification model; (b) CNN-based particle morphology identification model; (c) BiLSTM-based mechanical responses prediction model; (d) BiLSTM-based induced fabric anisotropy prediction model

Fig. 7 Feature maps in the first four layers of CNN-based PSD identification model

Fig. 8 Predicted PSD curves on the testing set

Fig. 9 Classification of mixture ratios on the testing set

Fig. 10 Predicted relationships of $p-\varepsilon$, $q-\varepsilon$ and $e-\varepsilon$ on the testing set

Fig. 11 Predicted relationships of $a-\varepsilon$, $a_n-\varepsilon$ and $a_s-\varepsilon$ on the testing set

Fig. 12 Predicted relationships on the unknown samples with new particle morphology: (a) mechanical responses; (b) induced anisotropy

Fig. 13 Predicted anisotropy for a dense sample R10_T90 using BiLSTM

1
2
3
4
5
6
7
8
9
10
11
12
13
14
15
16
17
18
19
20
21
22
23
24
25
26
27
28
29
30
31
32
33
34
35
36
37
38
39
40
41
42
43
44
45
46
47
48
49
50
51
52
53
54
55
56
57
58
59
60
61
62
63
64
65

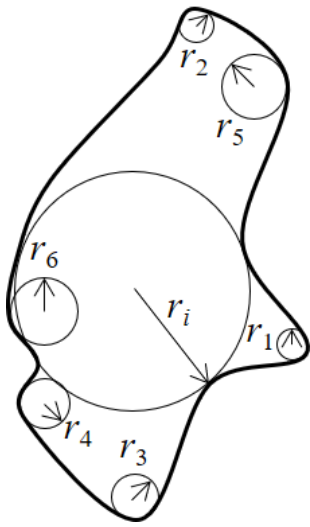


Fig. 1 Definition of particle circularity and roundness

1
2
3
4
5
6
7
8
9
10
11
12
13
14
15
16
17
18
19
20
21
22
23
24
25
26
27
28
29
30
31
32
33
34
35
36
37
38
39
40
41
42
43
44
45
46
47
48
49
50
51
52
53
54
55
56
57
58
59
60
61
62
63
64
65

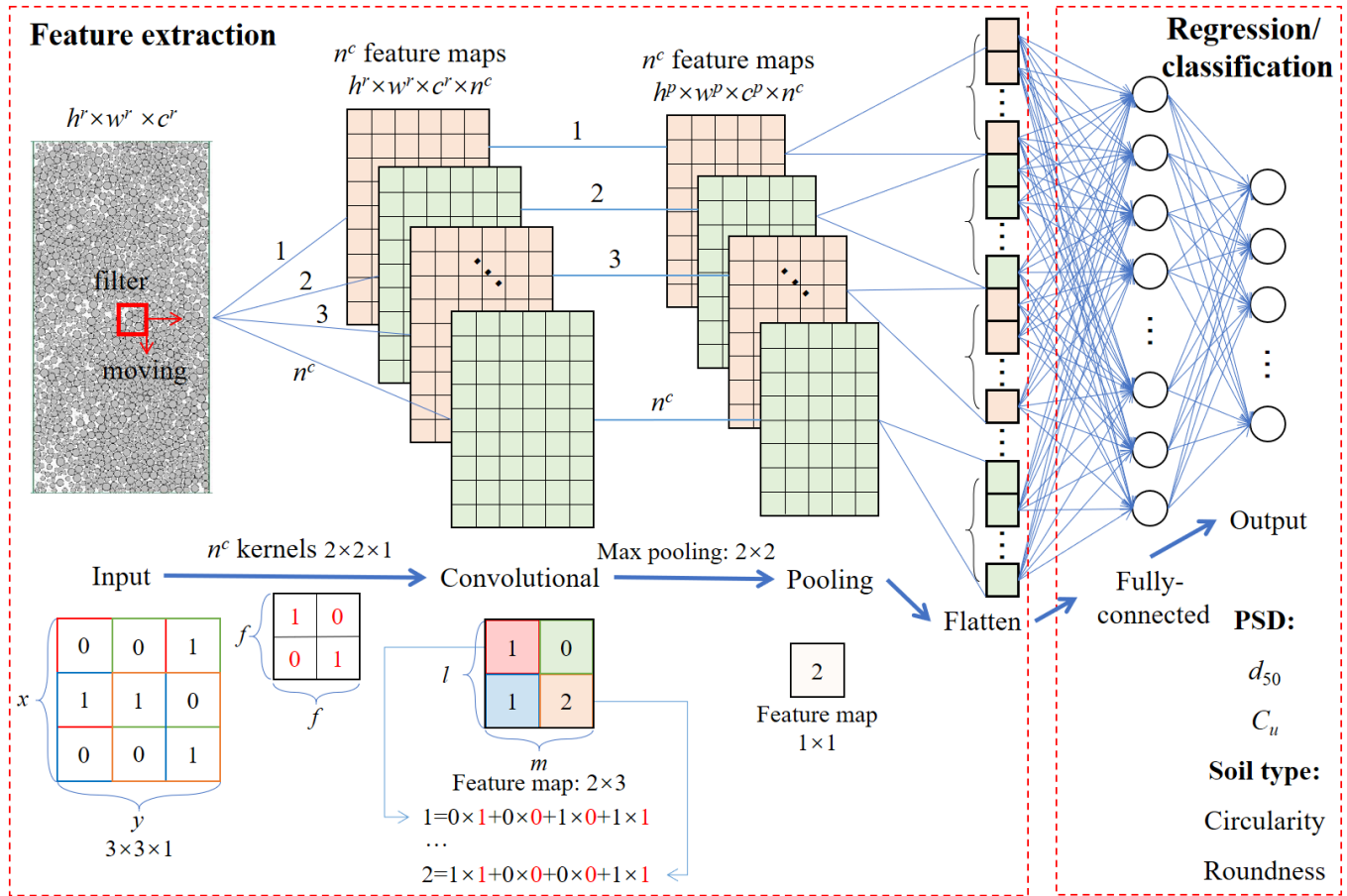


Fig. 2 Schematic view of CNN

1
2
3
4
5
6
7
8
9
10
11
12
13
14
15
16
17
18
19
20
21
22
23
24
25
26
27
28
29
30
31
32
33
34
35
36
37
38
39
40
41
42
43
44
45
46
47
48
49
50
51
52
53
54
55
56
57
58
59
60
61
62
63
64
65

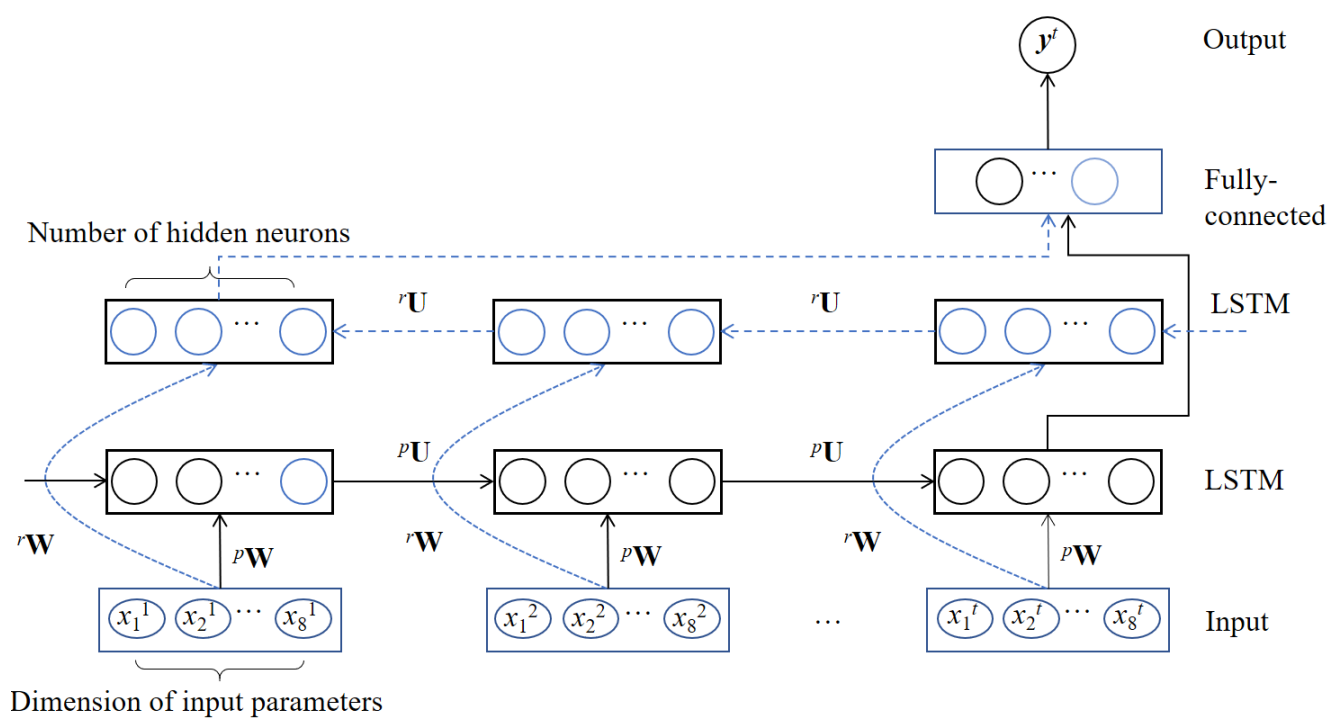


Fig. 3 Schematic view of BiLSTM

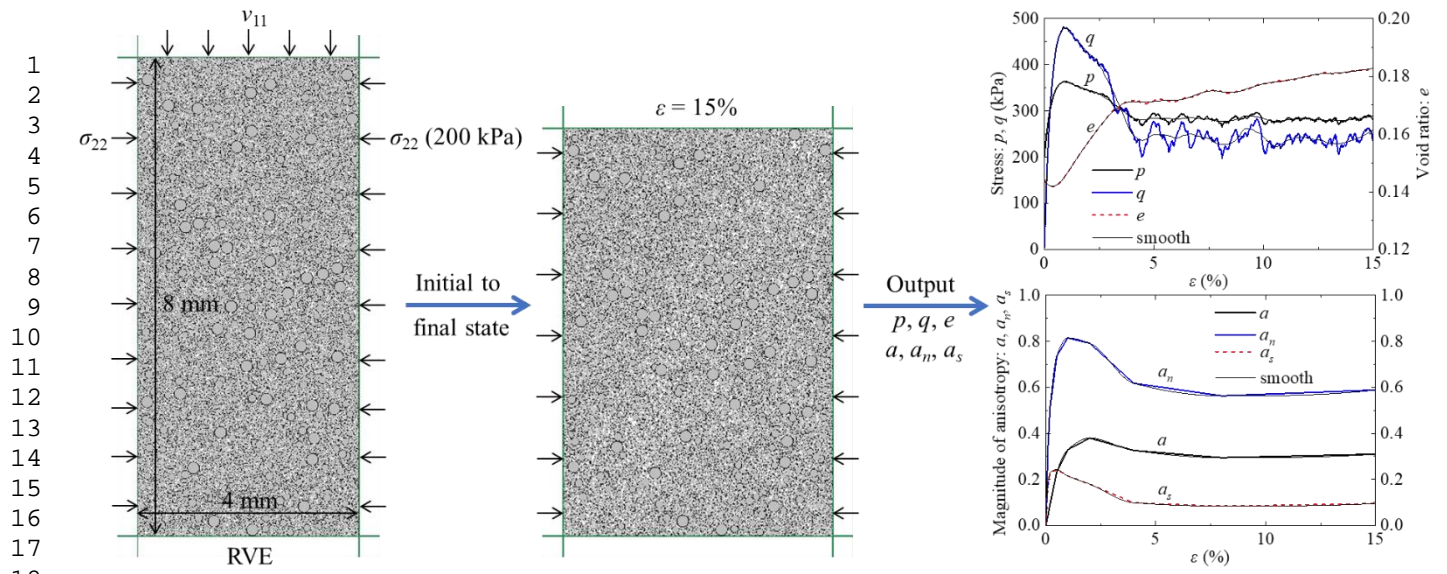


Fig. 4 A representative numerical biaxial test for 2D granular assembly and modelling results

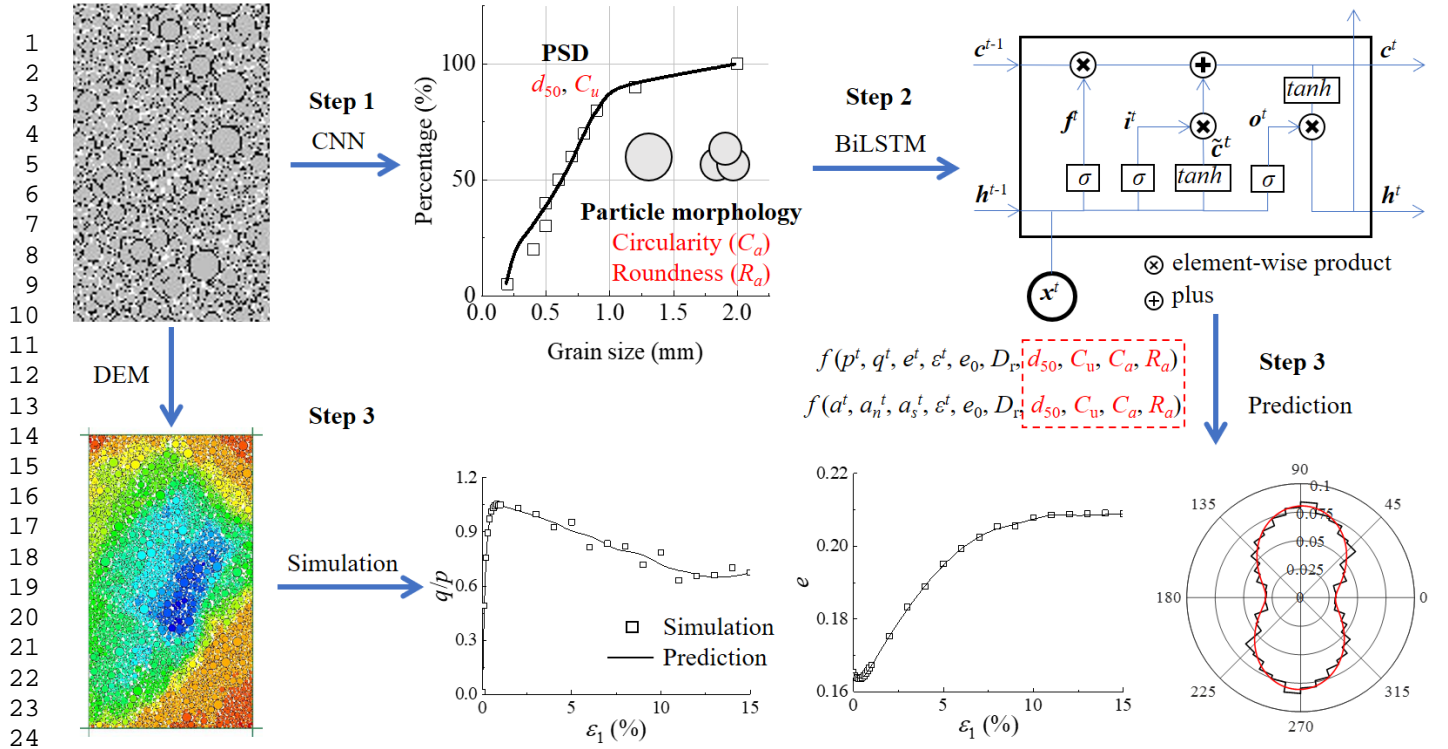


Fig. 5 Flowchart of the proposed DL based modelling framework

1
2
3
4
5
6
7
8
9
10
11
12
13
14
15
16
17
18
19
20
21
22
23
24
25
26
27
28
29
30
31
32
33
34
35
36
37
38
39
40
41
42
43
44
45
46
47
48
49
50
51
52
53
54
55
56
57
58
59
60
61
62
63
64
65

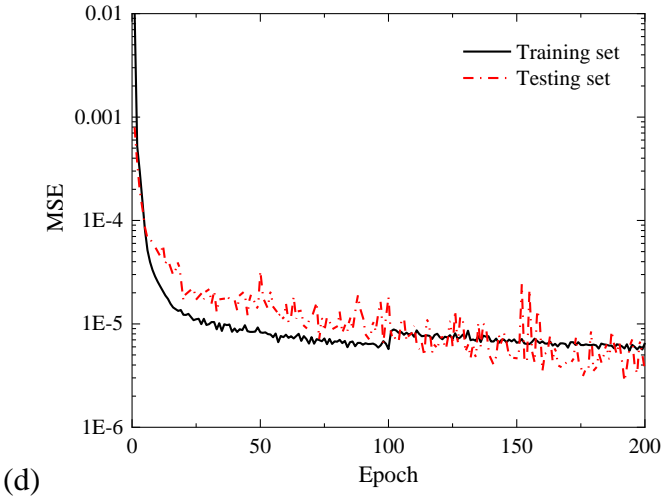
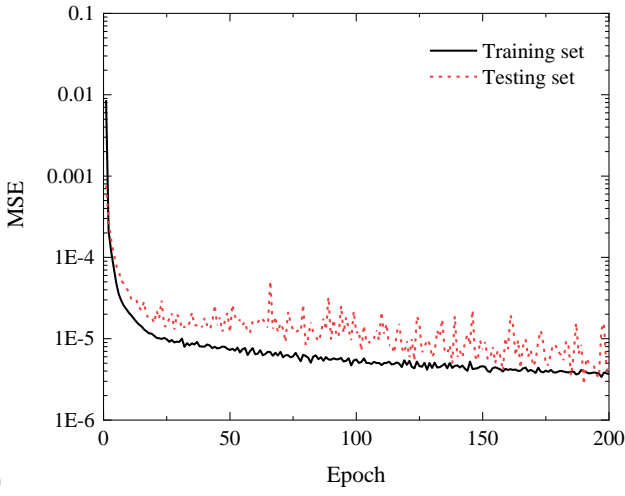
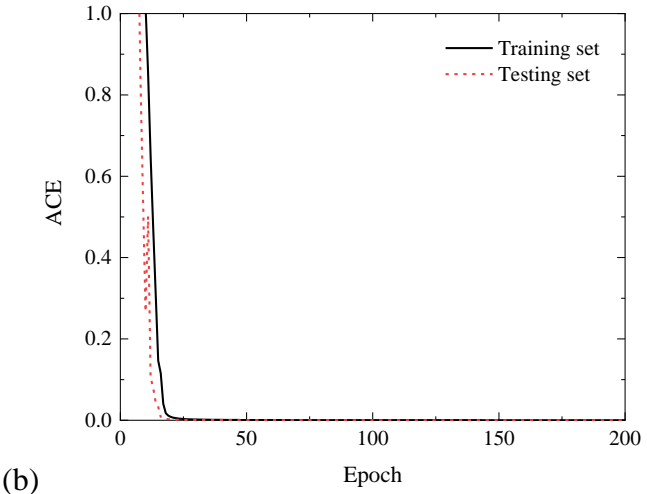
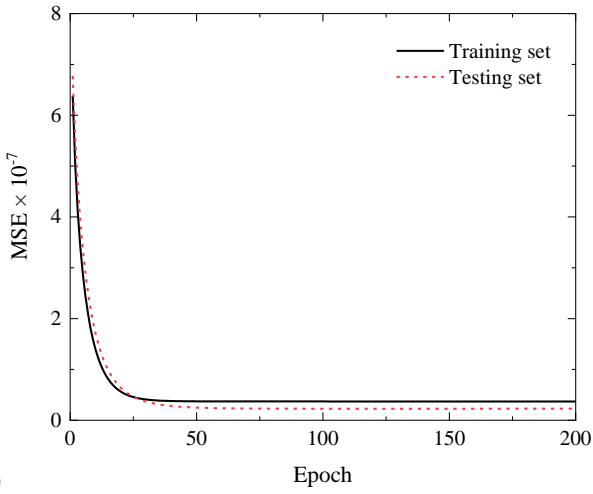


Fig. 6 Evolution of loss value: (a) CNN-based PSD identification model; (b) CNN-based particle morphology identification model; (c) BiLSTM-based mechanical responses prediction model; (d) BiLSTM-based induced fabric anisotropy prediction model

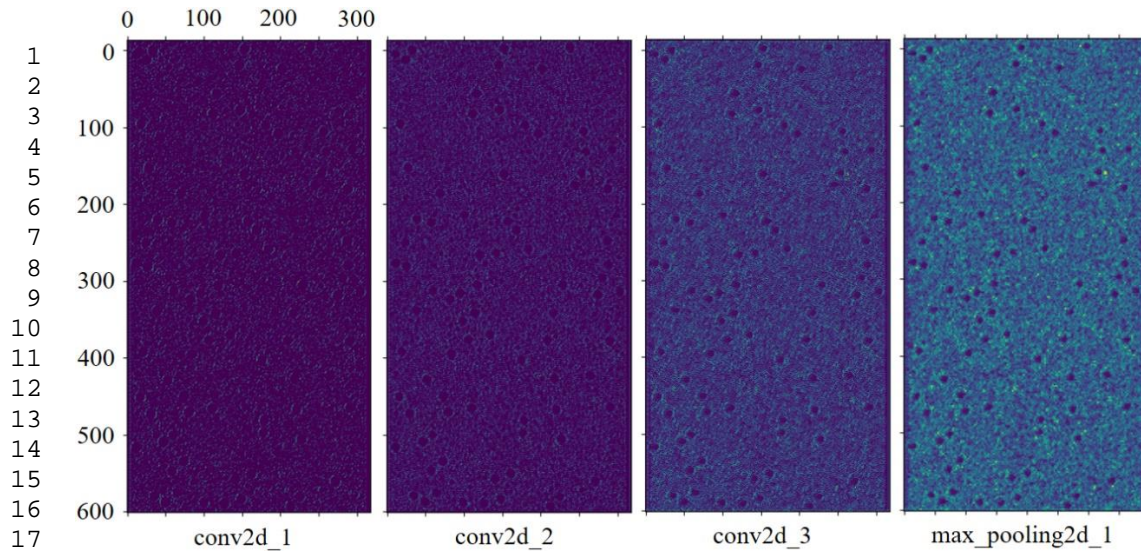


Fig. 7 Feature maps in the first four layers of CNN based PSD identification model

17
18
19
20
21
22
23
24
25
26
27
28
29
30
31
32
33
34
35
36
37
38
39
40
41
42
43
44
45
46
47
48
49
50
51
52
53
54
55
56
57
58
59
60
61
62
63
64
65

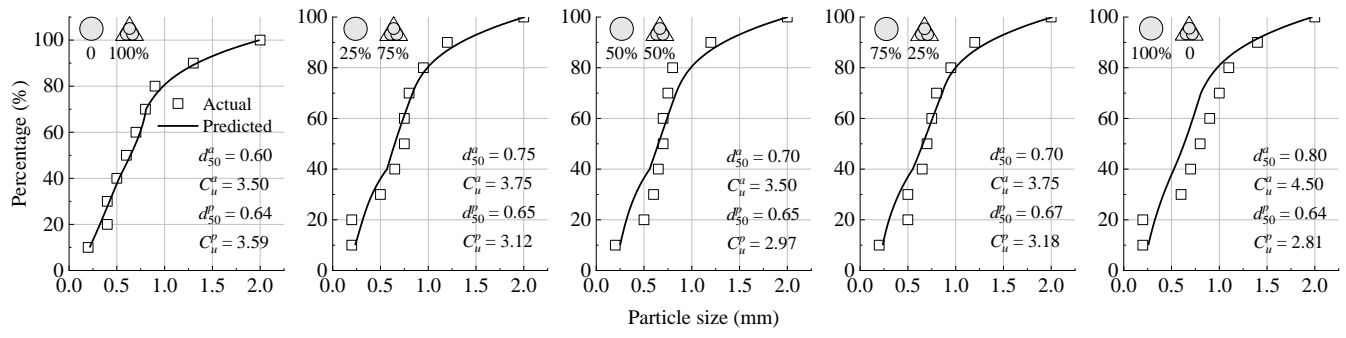


Fig. 8 Predicted PSD curves on the testing set

1
2
3
4
5
6
7
8
9
10
11
12
13
14
15
16
17
18
19
20
21
22
23
24
25
26
27
28
29
30
31
32
33
34
35
36
37
38
39
40
41
42
43
44
45
46
47
48
49
50
51
52
53
54
55
56
57
58
59
60
61
62
63
64
65

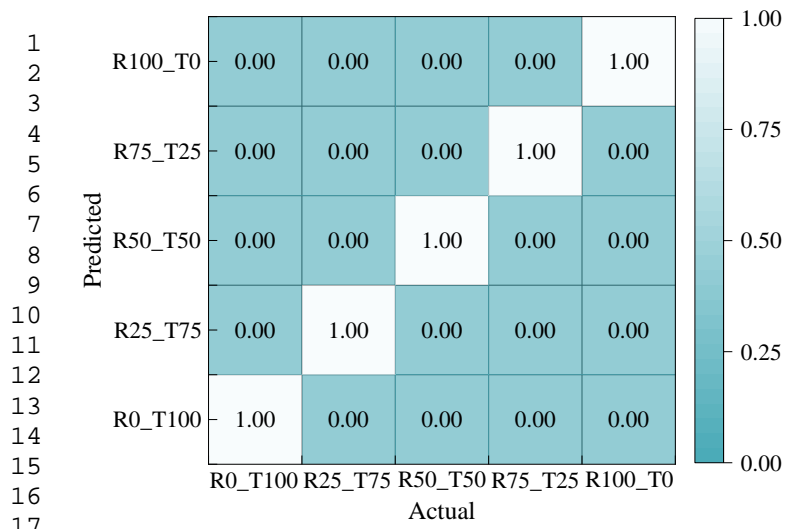


Fig. 9 Classification of mixture ratios on the testing set

1
2
3
4
5
6
7
8
9
10
11
12
13
14
15
16
17
18
19
20
21
22
23
24
25
26
27
28
29
30
31
32
33
34
35
36
37
38
39
40
41
42
43
44
45
46
47
48
49
50
51
52
53
54
55
56
57
58
59
60
61
62
63
64
65

1
2
3
4
5
6
7
8
9
10
11
12
13
14
15
16
17
18
19
20
21
22
23
24
25
26
27
28
29
30
31
32
33
34
35
36
37
38
39
40
41
42
43
44
45
46
47
48
49
50
51
52
53
54
55
56
57
58
59
60
61
62
63
64
65

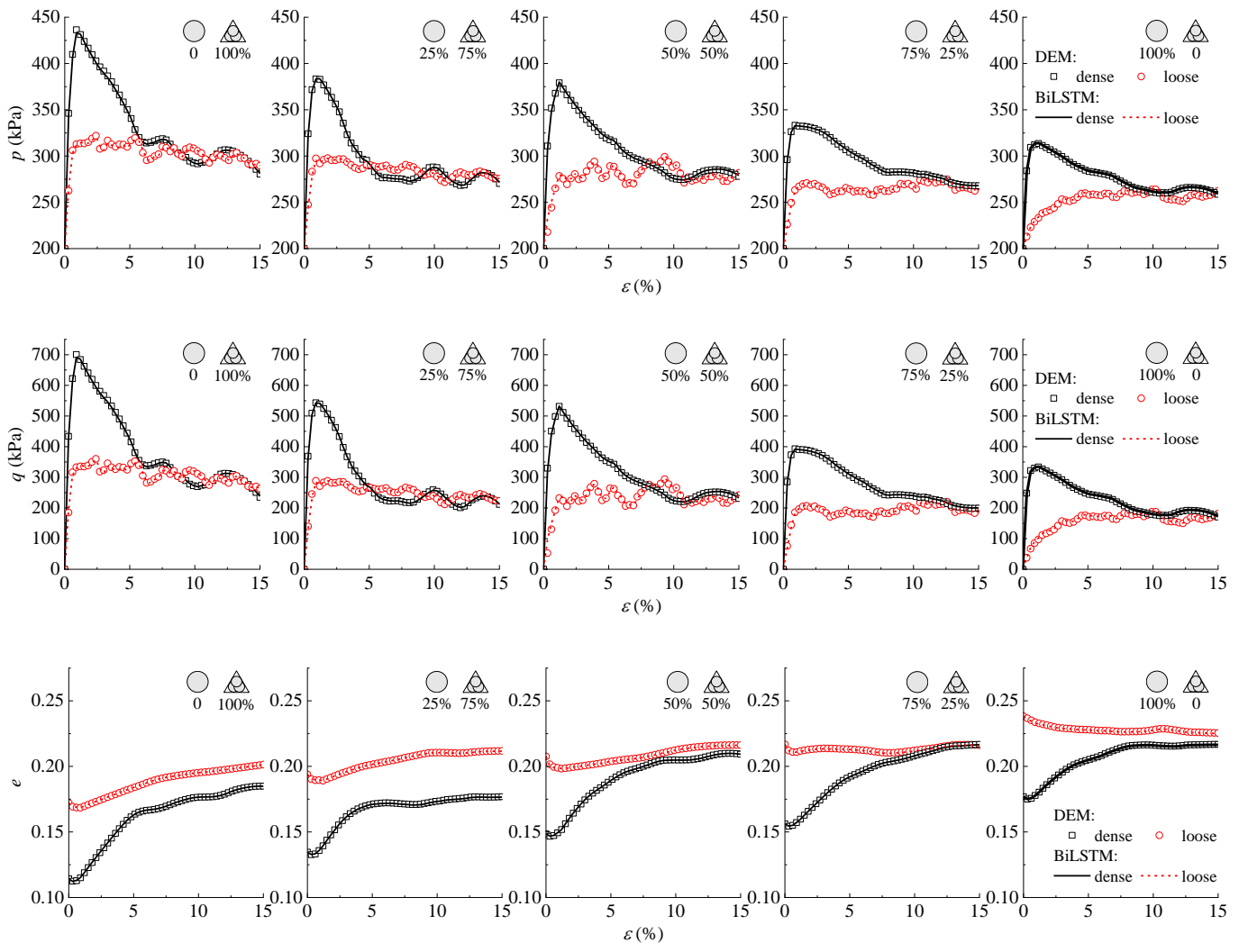


Fig. 10 Predicted relationships of $p-\epsilon$, $q-\epsilon$ and $e-\epsilon$ on the testing set

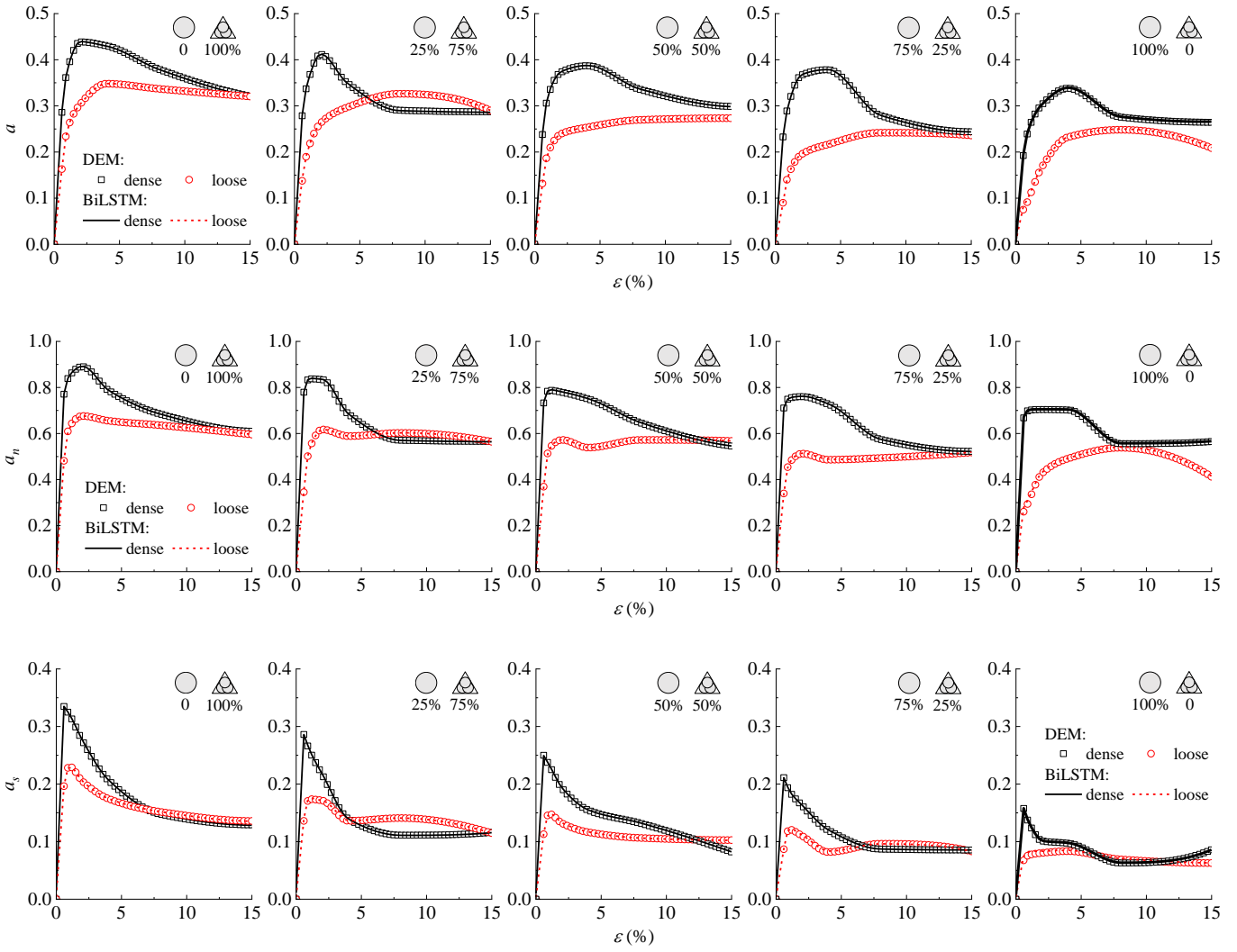


Fig. 11 Predicted relationships of $a-\epsilon$, $a_n-\epsilon$ and $a_s-\epsilon$ on the testing set

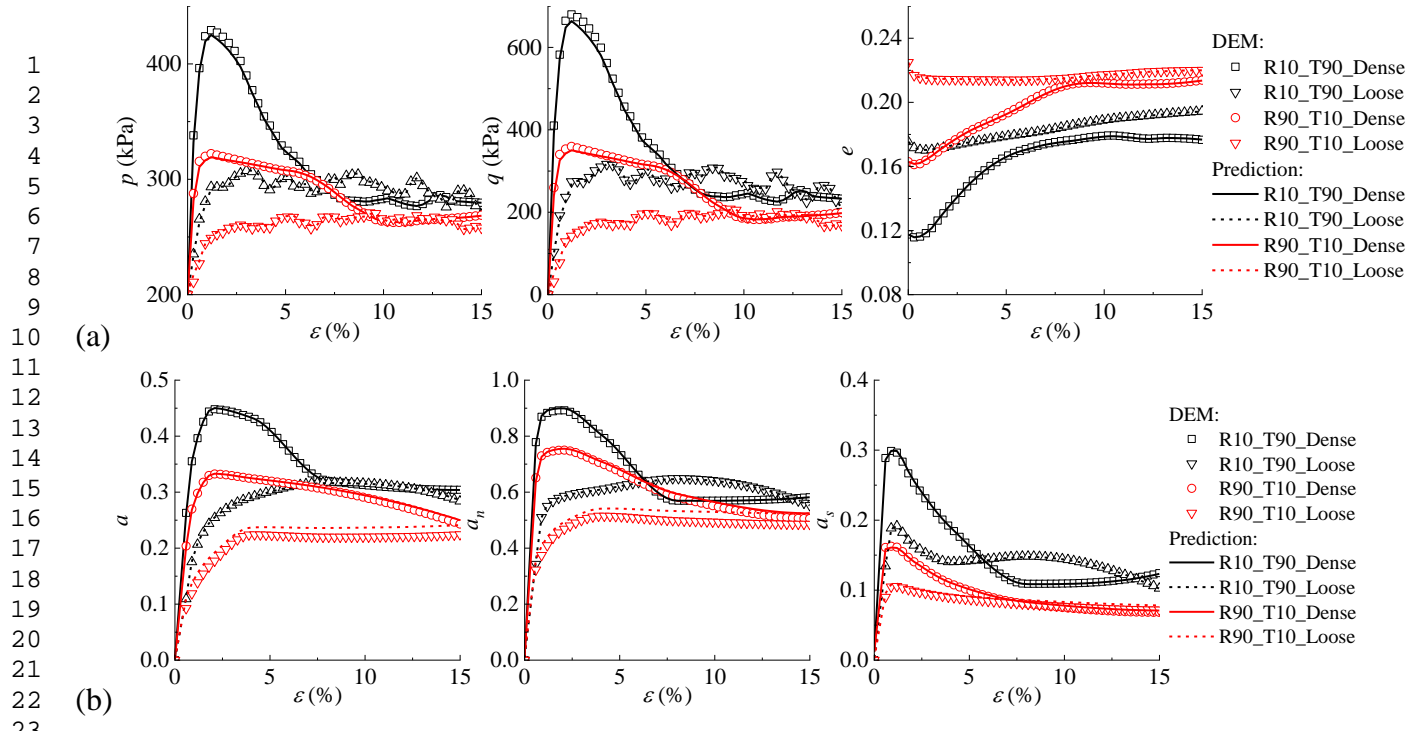


Fig. 12 Predicted relationships on the unknown samples with new particle morphology: (a) mechanical responses; (b) induced anisotropy

1
2
3
4
5
6
7
8
9
10
11
12
13
14
15
16
17
18
19
20
21
22
23
24
25
26
27
28
29
30
31
32
33
34
35
36
37
38
39
40
41
42
43
44
45
46
47
48
49
50
51
52
53
54
55
56
57
58
59
60
61
62
63
64
65

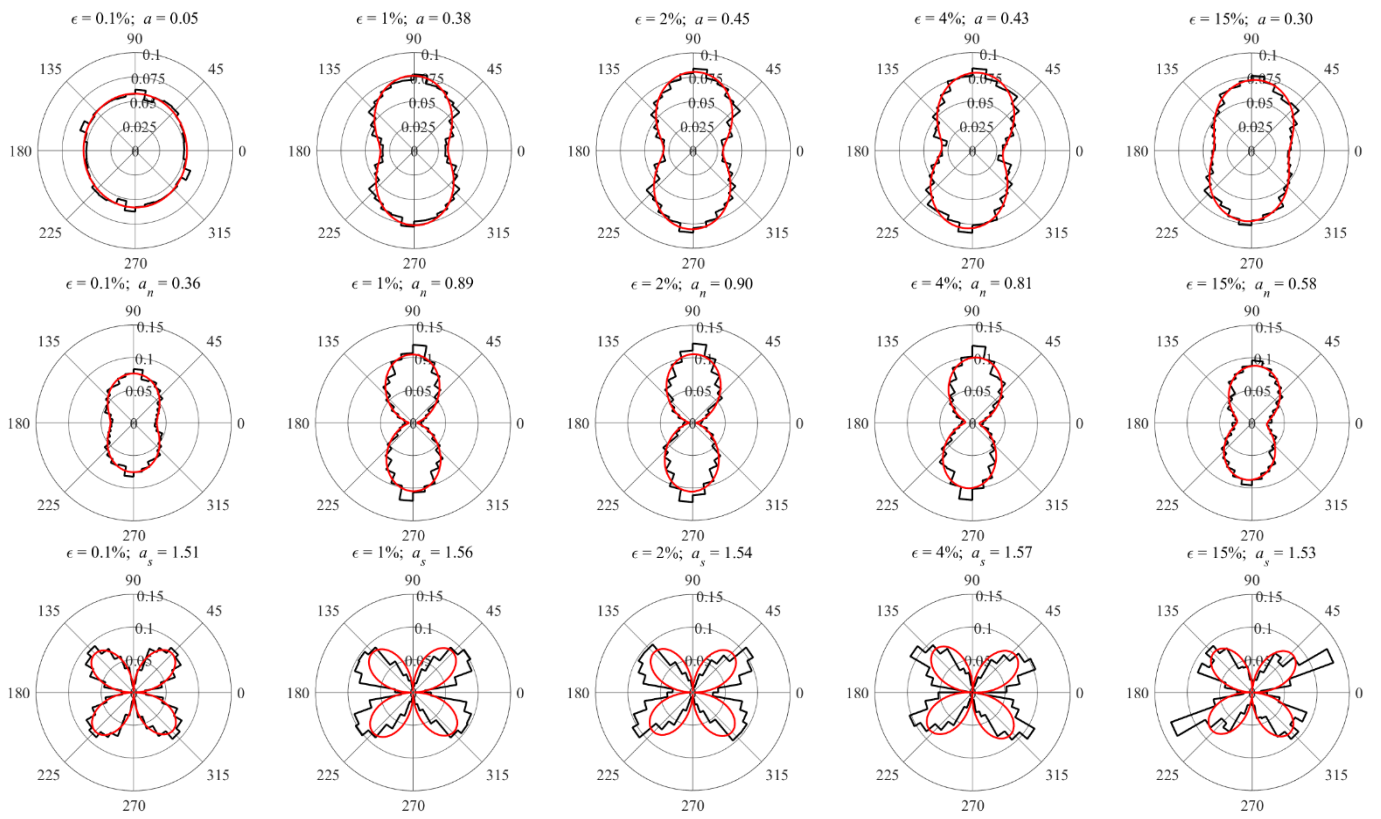


Fig. 13 Predicted anisotropy for a dense sample R10_T90 using BiLSTM